Evolution of Intrinsic Magnetic Properties in L1₀ Mn-Al Alloys Doped with Substitutional Atoms and Correlated Mechanism: Experimental and Theoretical Studies

Shuang Zhao, Yuye Wu,[*] Zhengying Jiao, Yuxiao Jia, Yichen Xu, Jingmin Wang, Tianli Zhang,[†] and Chengbao Jiang

Key Laboratory of Aerospace Materials and Performance (Ministry of Education), School of Materials Science and Engineering, Beihang University, 100191 Beijing, People's Republic of China

L1₀ MnAl permanent-magnet alloys are promising candidates to plug the gap in performance and applications between rare-earth permanent magnets and ferrites; doping with a third atom is essential to achieve decent magnetic properties and good L1₀-phase stability. In this work, the influence of substitutional atoms on intrinsic magnetic properties in L1₀ MnAl alloys is investigated by combined experimental and theoretical studies. A highly pure L1₀ phase is synthesized in $Mn_{55}Al_{45-x}M_x$ ($M =$ Co, Cu, Ga) alloys by regulation of the heat treatment, on the basis of ternary phase diagrams. It is demonstrated by experimental measurements and calculations that Cu and Co tend to enter 1a (0, 0, 0) sites, where they degrade the intrinsic magnetic properties of the alloys, and Ga prefers the 1d (1/2, 1/2, 1/2) sites, where it improves them. The excess valence electrons of Cu or Co compared with Mn lead to stronger bonding with Al, resulting in the preference of occupying 1a (0, 0, 0) sites. The similar valence-electron structure of Ga compared with Al makes Ga tend to occupy 1d (1/2, 1/2, 1/2) sites. On the basis of this understanding, we propose a strategy of replacing the antiferromagnetic Mn atoms by $3d$ atoms with fewer valence electrons than Mn, which may effectively enhance the intrinsic magnetic properties. Moreover, the stability of the alloyed L1₀ phase is investigated; Co is found to degrade the stability of the phase, but the addition of Cu or Ga can stabilize it. These results provide guidance for further performance optimization and composition design of Mn-based rare-earth permanent magnets.

I. INTRODUCTION

L1₀ MnAl permanent-magnet alloys have attracted renewed attention in recent years due to their interesting intrinsic magnetic properties, including saturation magnetization $M_s > 0.7$ MA/m, magnetic anisotropy $K_1 > 1.5$ MJ/m³, and Curie temperature $T_C > 600$ K [1–5]. Therefore, they are potential candidates to plug the performance gap between the expensive rare-earth-based magnets and the low-performance ferrites in various practical applications [6–12]. The L1₀ phase (also called the "τ phase" [13–15]) is the sole ferromagnetic phase in the Mn-Al binary system; it has an *ordered* face-centered-tetragonal (FCT)-type structure of $P4/mmm$ symmetry [16]. An equivalent ordered body-centered-tetragonal (BCT)-type cell has the same c parameter, but a is reduced by $\sqrt{2}$. The transformation from FCT to BCT is shown in Fig. S1 in Supplemental Material [17].

For the ideal equiatomic and perfectly ordered $Mn_{50}Al_{50}$ composition, the Mn atoms occupy the 1a (0, 0, 0) sites

and interact ferromagnetically, while Al atoms occupy the 1d (1/2, 1/2, 1/2) sites and have a negligible magnetic moment. However, the L1₀ phase cannot be obtained in alloys with stoichiometric composition; it is formed within a narrow window of the nonstoichiometric composition $Mn_{50+x}Al_{50-x}$ ($1 \le x \le 8$). In this case, the excess Mn atoms also enter 1d (1/2, 1/2, 1/2) sites, and interact antiferromagnetically with the nearest-neighbor Mn at the 1a sites [10,18,19]. Even in the Mn-rich composition range, the L1₀ phase is still thermodynamically metastable. It is prone to decompose into the thermodynamically stable but nonmagnetic β-Mn phase ($P4_132$, Mn $cP20$ type) and γ_2 phase ($R3m$, Al_8Cr_5 type) [20–22]. Therefore, researchers hoped to use elemental alloying to stabilize the L1₀ phase without degrading the intrinsic magnetization. However, there is always a trade-off between intrinsic magnetism and ferromagnetic phase stability of alloyed Mn-Al materials. Small atoms such as carbon (rC $= 0.77$ Å, rMn $= 1.26$ Å, rAl $= 1.43$ Å) are inclined to occupy octahedral interstitial sites in the L1₀ lattice. It has been widely recognized that the addition of interstitial carbon atoms is effective in stabilizing the L1₀ phase [23–28] but it gives rise to a drastic

*wuyuye@buaa.edu.cn
†tlzhang@buaa.edu.cn

decline of intrinsic magnetic properties such as the Curie temperature and magnetic anisotropy [18,27,29]. Recently, we attempted to dope the $L1_0$ phase with rare-earth atoms, which have strong spin-orbit interactions and larger atomic radii (the atomic radii range from 1.75 to 1.83 Å) [30]. Because of the large atomic size difference (size deviation approximately 50%), the rare-earth atoms can hardly enter the $L1_0$ lattice to substitute the Mn or Al sites, so it is difficult to regulate the intrinsic magnetic properties of $L1_0$ MnAl alloys through doping with large atoms. Therefore, by seeking appropriate atoms that have an atomic radius comparable to that of Mn or Al, it may be possible to regulate the intrinsic magnetic properties of $L1_0$ MnAl significantly; substitutional elements are the most promising candidates. Many substitutional atoms have been studied. Mican *et al.* [31,32] investigated the effect of Ni on the magnetic properties, but a pure $L1_0$ phase was hard to obtain. Manchanda *et al.* [33,34] reported theoretical calculations showing that the substitution of Fe for Mn significantly degrades the magnetization of Mn-Al alloys. There is a lack of a systematic investigations of the influence of substitutional elements on the intrinsic magnetism of Mn-Al alloys, and the corresponding mechanisms need to be properly understood. A combination of experiments and theoretical calculations is required to establish the criteria for selecting proper elements.

In this work, we choose two types of elements for study: one is a 3*d* metal (Cu or Co) that has a radius similar to that of Mn; the other is Ga, a typical *sp* main-group element that also forms a ferromagnetic $L1_0$ alloy with Mn. The atomic radius and valence electronic structure of these elements are summarized in Fig. 1. Firstly, these three atoms have completely different magnetic properties and electronic structures, and they are expected to have different effects on the intrinsic magnetism of the $L1_0$ phase. Cu and Co are representative 3*d* elements that are commonly used to regulate magnetism in materials such as Heusler alloys. Co has the strongest ferromagnetism and has a $3d^7s^2$ valence-electron structure, whereas Cu has a full 3*d* shell and is nonmagnetic. Secondly, Cu and Co have radii similar to the radius of Mn, and Ga has a radius similar to that of Al, so these characteristics make them good candidate substitutional atoms to occupy $L1_0$ lattice sites. Thirdly, the ferromagnetic $L1_0$ phase is metastable; the preparation of the $L1_0$ phase is complicated and it varies significantly with a slight change of chemical composition. On the basis of numerous experimental results, a high-purity $L1_0$ phase can be obtained in Mn-Al magnetic

alloys doped with a certain amount of Co, Cu, Ga, but it is difficult to obtain in Cr-, Zn-, or V-doped Mn-Al alloys. To obtain a pure $L1_0$ phase, to analyze the experimental and theoretical results accurately, Co, Cu, and Ga are selected.

We systematically investigate the influence of doping with these substitutional atoms on the intrinsic magnetic properties of the $L1_0$ phase. On the basis of an understanding of the evolution of the magnetic properties of the alloyed $L1_0$ phase, a future optimization scheme is proposed. Our results provide guidance for further performance optimization and composition design.

II. EXPERIMENTAL PROCEDURE

Binary $Mn_{55}Al_{45}$ and ternary $Mn_{55}Al_{45-x}M_x$ (M = Cu, Ga: x = 3, 6, M = Co: x = 2, 4) alloys are prepared by our arc melting appropriate quantities of elemental materials. Excess Mn up to 5 wt % is added to compensate for the loss of Mn during melting. Homogenization and annealing are done in quartz tubes backfilled with 0.2-bar Ar. The $Mn_{55}Al_{45-x}Co_x$ (x = 2, 4) and $Mn_{55}Al_{45-x}Cu_x$ (x = 3, 6) alloys are homogenized at 1273 K for 12 h and then quenched in 5% salt brine to obtain a high-purity ϵ phase ($P6_3/mmc$, $hP2$ type); we use "A3 phase" in the following text [32]. Subsequently, the A3 ingots are annealed at 723 K for 30 min to obtain the $L1_0$ phase. The binary $Mn_{55}Al_{45}$ and ternary $Mn_{55}Al_{45-x}Ga_x$ (x = 3, 6) alloys are homogenized at 1273 K for 12 h and cooled in air. The ternary (Mn, Al)Ga specimens are further annealed at 773 K for 24 h [21,37]. The crystal structure is identified with a Rigaku D/max-2500 X-ray diffractometer with use of Cu $K\alpha$ radiation (λ = 1.5418 Å). Magnetic measurements are performed with a physical property measurement system (PPMS, Quantum Design) with an applied field up to 90 kOe. Thermomagnetic data are collected with a VSM (HH-15, Nanjing University Instrument Plant) with an applied field of 10 kOe. The density of all the alloys is measured with a gas-displacement pycnometry system (AccuPyc II 1340, Micromeritics Instrument Corporation). The nominal compositions are checked by electron probe microanalysis (JXA-8100, JEOL) using an energy-dispersive-spectrometer analysis system.

First-principles computations are performed with VIENNA AB INITIO SIMULATION PACKAGE [38] on the basis of density-functional theory with the projector-augmented-wave method [39] to describe the election-ion interaction. The generalized-gradient-approximation exchange-correlation energy designed by Perdew *et al.* [40] is used
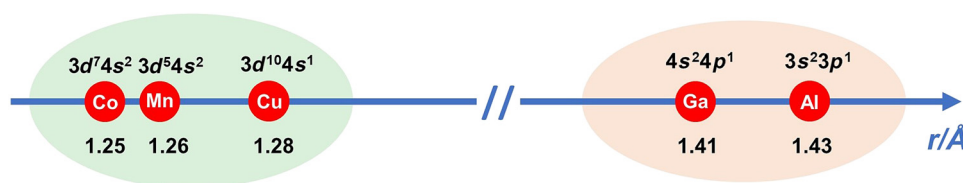

FIG. 1. Atomic radii and valence-electron structures of Mn, Al, Co, Cu, and Ga [35].

for the description of exchange and correlation effects. The structures are optimized by the conjugate-gradient method with force convergence lower than 10^{-3} eV/Å and energy convergence lower than 10^{-6} eV per atom. The integrations in the Brillouin zone are performed with k-point grids of $7 \times 7 \times 7$. For all the calculations, the experimental lattice parameters of binary Mn-Al alloy were used ($a = 2.777$ Å, $c = 3.571$ Å).

III. RESULTS AND DISCUSSION

A. Synthesis of the $L1_0$ phase in the $Mn_{55}Al_{45-x}M_x$ ($M =$ Co, Cu, Ga) alloy systems

The $L1_0$ phase can be obtained only by water quenching of the A3 phase followed by annealing, or cooling of the A3 phase at an appropriate rate [41,42]. Therefore, the first step is to obtain a pure A3 phase. However, the respective phase region of A3 and $L1_0$ is likely to change with the third dopant element. Figures 2(a) and 2(d) show the schematic ternary phase diagrams of the Al-Co-Mn system at 1273 K and the Al-Cu-Mn system at 1223 K, respectively [43]. In the Al-Co-Mn ternary system, the A3-phase region significantly shrinks with increasing Co dopant, and the boundary of the A3 phase is at approximately 2 at. % Co when the Mn content is 55 at. %, and a δ' phase ($Pm\bar{3}m$,

CsCl type, structure symbol B2) appears in the region with higher Co content. For the Al-Cu-Mn ternary system, the A3-phase region is slightly expanded by the Cu dopant, which means that the A3 phase can be obtained over quite a large composition range (0 at. % $\le \omega Cu \le 10$ at. % at 55 at. % Mn), and a β phase ($Pm\bar{3}m$, CsCl type, also a B2 phase) appears when the Cu content exceeds 10 at. %. The composition points for Co- or Cu-doped alloys are indicated by different symbols in the ternary diagram, as shown in Figs. 2(a) and 2(d). However, the conventional approach to obtain the $L1_0$ phase, mentioned above, does not work for Co- or Cu-doped alloys [36]. Other equilibrium phases were formed after water quenching or cooling of the A3 phase directly, indicating the phase region of the A3 phase gradually shrinks with decreasing temperature. Figure S2 in Supplemental Material [17] shows XRD patterns of Cu- or Co-doped alloys that are quenched in water after homogenization. Therefore, we decided to quench the alloyed specimens in 5% salt brine to freeze the high-temperature A3 phase at room temperature, followed by a low-temperature anneal to obtain the $L1_0$ phase. The heat-treatment process is described by temperature-time curves in the insets in Figs. 2(b), 2(c), 2(e), and 2(f). Figure 2(b) shows the XRD patterns of Co-doped alloys after salt brine quenching. The 2 at. % Co alloy can be obtained in the
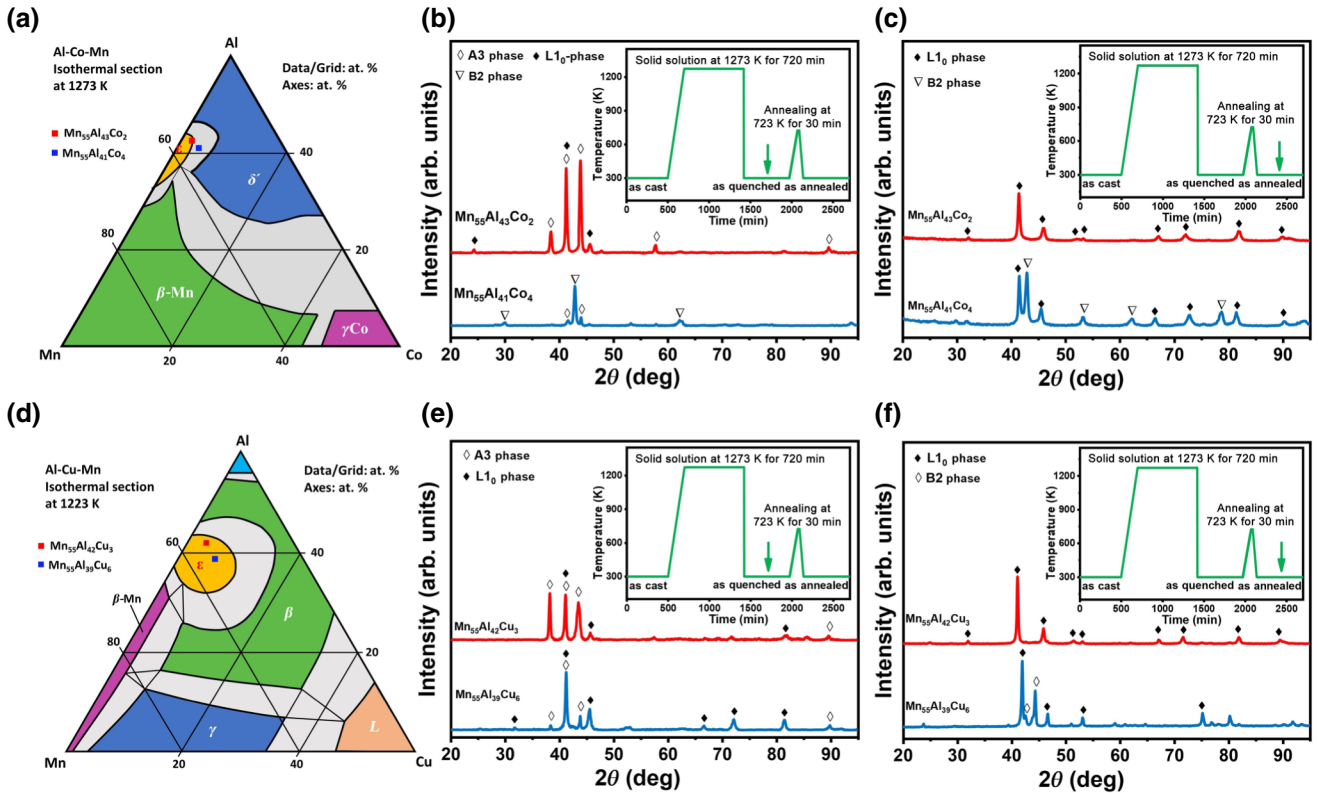

FIG. 2.   (a) Al-Co-Mn isothermal ternary phase diagram at 1273 K [42]. Room-temperature XRD patterns of (b) as-quenched and (c) as-annealed $Mn_{55}Al_{45-x}Co_x$ ($x = 2, 4$) ingots. (d) Al-Cu-Mn isothermal ternary phase diagram at 1223 K [42]. Room temperature XRD patterns of (e) as-quenched and (f) as-annealed $Mn_{55}Al_{45-x}Cu_x$ ($x = 3, 6$) ingots.

almost-pure A3 phase, but there is a small fraction of $L1_0$. When the Co concentration increases to 4 at. %, a considerable amount of the B2 phase appears [44,45]. Annealing treatment at 723 K for 30 min transforms the A3 phase to the $L1_0$ phase, but the B2 phase remains in the 4 at. % Co alloy, as shown in Fig. 2(c). Similarly, Figs. 2(e) and 2(f) show XRD patterns of the quenched and postannealed states of $Mn_{55}Al_{45-x}Cu_x$ ($x = 3$, 6) alloys. The same quenching procedure leads to the coexistence of the A3 and $L1_0$ phases. After annealing, the $Mn_{55}Al_{42}Cu_3$ specimen is a high-purity $L1_0$ phase, while in the $Mn_{55}Al_{39}Cu_6$ alloy some B2 phase accompanies the $L1_0$ phase.

$Mn_{55}Al_{45}$ and $Mn_{55}Al_{45-x}Ga_x$ ($x = 3$, 6) alloys can be treated by the conventional method: homogenization at 1273 K for 12 h and cooling in air. After heat treatment, a single $L1_0$ phase is obtained for $Mn_{55}Al_{45}$, while a mixture of major $L1_0$ phase and minor γ_2 phase is formed in the ternary (Mn, Al)Ga alloys, as shown in Fig. 3(a). Therefore, postannealing at 773 K for 24 h is performed on the two ternary specimens, and the residual γ_2 phase transforms to the $L1_0$ phase, as indicated by the disappearance of the diffraction peaks in Fig. 3(b). This transformation was also reported in Ga-doped Mn-Al systems by Mix *et al.* [21].

In summary, the $L1_0$ phase is obtained in $Mn_{55}Al_{45}$, $Mn_{55}Al_{42}Ga_3$, $Mn_{55}Al_{39}Ga_6$, $Mn_{55}Al_{42}Cu_3$, and $Mn_{55}Al_{43}Co_2$ specimens by regulation of the heat-treatment process. In the $Mn_{55}Al_{41}Co_4$ and $Mn_{55}Al_{39}Cu_6$ alloys, with a higher level of the dopant element, the phase structure contains a major $L1_0$ phase and small amount of a second phase. A summary of the heat-treatment process and the phase structure of $Mn_{55}Al_{45-x}M_x$ ($M = $ Cu, Co, Ga) alloys is given in Table S1 in Supplemental Material [17]. The chemical compositions of the $L1_0$ and B2 phases of $Mn_{55}Al_{45-x}M_x$ ($M = $ Co, Cu, Ga) alloys detected by energy-dispersive spectroscopy are summarized in Table S2 in Supplemental Material [17]. Detailed information on the crystal structure and phase fractions of these specimens is provided in Table S3 in Supplemental Material [17].

B. Intrinsic magnetic properties

Magnetic measurements are performed on $Mn_{55}Al_{45-x}M_x$ ($M = $ Cu, Co, Ga) alloys to reveal the effect of doping with substitutional atoms on the intrinsic magnetic properties, including the saturation magnetization (M_s), uniaxial anisotropy (K_1), and Curie temperature (T_C), as shown in Figs. 4 and 5. Figure 4(a) shows the mass-magnetization curve of undoped and doped $L1_0$ specimens measured at 300 K. Figure 4(b) shows the volume magnetization calculated with the alloy density (see Table S4 in Supplemental Material for the alloy density). All the alloys exhibit ferromagnetism. M_s and K_1 are calculated from 9-T magnetization curves by the approach-to-saturation method. The high-field

data are fitted to $M = M_s[1 - (b/H^2)] + \chi H$ and $b = (4K_1^2/15\mu_0^2M_s^2)$ [46–48], where M_s, b, and χ are the saturation magnetization, a constant related to K_1^2, and the high-field susceptibility, respectively. The latter can be ignored when the field is not very strong. According to the formulae, we extract the approach-to-saturation segment of the magnetization curves and make a linear fit of M_H versus $1/H^2$; the intercept on the y axis is M_s, and the slope is $-bM_s$. Then we can calculate K_1 from M_s and b. We select $Mn_{55}Al_{45}$ and $Mn_{55}Al_{42}Ga_3$ to illustrate the calculation process and results, as shown in Figs. 4(c) and 4(d), respectively. The linear-regression coefficient R^2 is greater than 0.99 for all the alloys, indicating a near-perfect linear relationship, resulting in reliable values of K_1. The variation of M_s at 300 K with increasing dopant concentration is summarized in Fig. 4(e). We can observe that the variation falls into two categories: one for Cu and Co and the other for Ga. In the first case, M_s exhibits a significant linear decrease with increasing substitution of Cu or Co for Al. The rate of decrease rate of M_s is almost the same for nonmagnetic Cu and ferromagnetic Co; the value is large, about 10 Am^2/kg per 1 at. % atom dopant. Both the volume magnetization and the mass magnetization behave similarly.

However, for the Ga-doped alloys, there is only a slight change of M_s; it decreases slightly from 126 Am^2/kg with no Ga to 117 Am^2/kg for 6 at. % Ga. The values of M_s per unit volume for ternary Ga-doped alloys are larger than those for the binary $Mn_{55}Al_{45}$ binary alloy, which can be attributed to the slight decrease of the mass magnetization and the increase of alloy density with increasing Ga content. According to the evolution of M_s of $Mn_{55}Al_{45-x}M_x$ ($M = $ Cu, Co, Ga) alloys, it is suggested that Co and Cu tend to occupy the same site in the $L1_0$ lattice, but Ga tends to occupy another site. The doping-element-concentration dependence of K_1 is summarized in Fig. 4(f). For binary $Mn_{55}Al_{45}$, the K_1 is 1.76 MJ/m^3, in accordance with previous literature [29,49]. The evolution of K_1 with the dopant concentration is the same as the variation of M_s for the doped Mn-Al alloys; it decreases significantly with the concentration of Cu or Co, but Co leads to a more obvious decrease. However, K_1 increases slightly with Ga doping, increasing from 1.76 MJ/m^3 for $Mn_{55}Al_{45}$ to 1.88 MJ/m^3 for $Mn_{55}Al_{39}Ga_6$. Moreover, for $Mn_{55}Al_{41}Co_4$, $Mn_{55}Al_{39}Cu_6$, and $Mn_{55}Al_{39}Ga_6$, M_s and K_1 are not characteristic of a single phase, and it is difficult to separate M_s and K_1 of each phase, because we cannot separate the contribution of each phase to whole of the magnetism. The magnetization of the $Mn_{55}Al_{41}Co_4$, $Mn_{55}Al_{39}Cu_6$, and $Mn_{55}Al_{39}Ga_6$ alloys is best regarded as an overall average. The K_1 values of the $Mn_{55}Al_{41}Co_4$, $Mn_{55}Al_{39}Cu_6$, and $Mn_{55}Al_{39}Ga_6$ alloys are also average values, defined as effective first-anisotropy constants, K_1^{eff}.

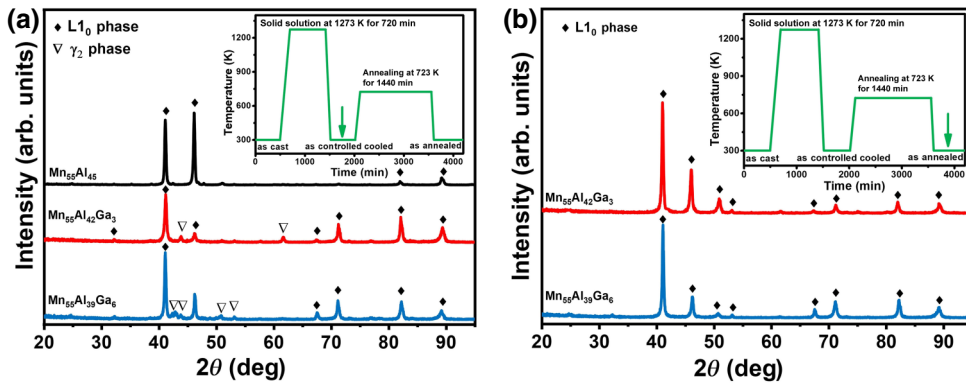The Curie temperatures (T_C) of these alloys is determined from the thermomagnetic curves, as shown in

FIG. 3. Room-temperature XRD patterns of (a) air-cooled and (b) as-annealed $Mn_{55}Al_{45-x}Ga_x$ ($x = 0, 3, 6$) alloys.

Fig. 5(a). The temperature dependence of the normalized magnetization ($M/M_{300\,K}$) of $Mn_{55}Al_{45-x}M_x$ ($M = Cu$, Co, Ga) alloys is measured from 300 to 700 K, and T_C is determined as the temperature where the first derivative (dM/dT) reaches its maximum negative value, as shown in the inset in Fig. 5(a). The influence of the type and concentration of dopant atoms on T_C is shown in Fig. 5(b). For all

the doped alloys, T_C also exhibits the same tendency as M_s and K_1, but in some cases two Curie temperatures are seen. For Co and Cu, T_C shows a slight decrease compared with that of the $Mn_{55}Al_{45}$ binary alloy, the rate of decrease ($v = |dM_s/dx|$) being greater for Co than for Cu. For Ga-doped alloys, T_C is higher than it is in $Mn_{55}Al_{45}$. Two different Curie temperatures are detected for $Mn_{55}Al_{41}Co_4$,
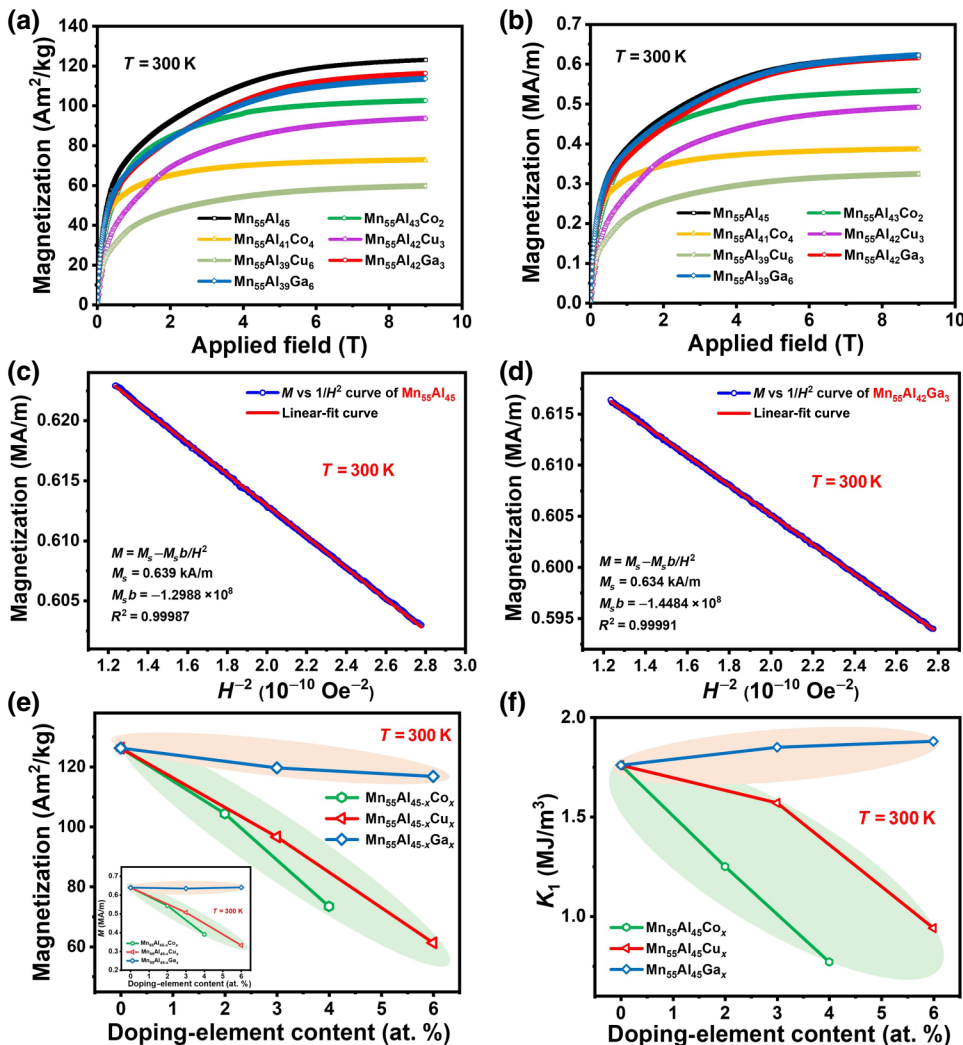

FIG. 4. (a) Mass-magnetization curves and (b) volume-magnetization curves of $Mn_{55}Al_{45-x}M_x$ ($M = Cu$, Co, Ga) samples up to 90 kOe at 300 K. (d),(d) Linear-fit curves of M^{-1}/H^2. (e) Saturation magnetization as a function of Co, Cu, and Ga content at 300 K. (f) K_1 as a function of Co, Cu, and Ga content at 300 K.
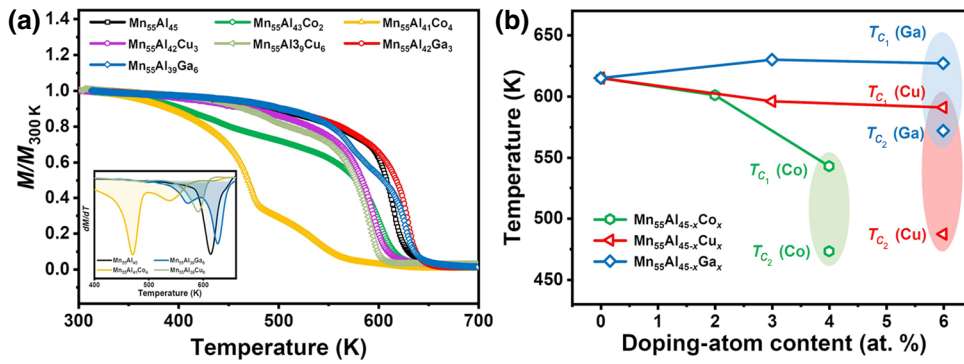
FIG. 5. (a) Temperature dependence of normalized magnetization ($M/M_{300\ K}$) for $Mn_{55}Al_{45-x}M_x$ ($M = $ Cu, Co, Ga). (b) Curie temperature as a function of Co, Cu, and Ga content.

$Mn_{55}Al_{39}Cu_6$, and $Mn_{55}Al_{39}Ga_6$. For the $Mn_{55}Al_{41}Co_4$ alloy, the Curie temperature of the $L1_0$ phase is 543 K, and the other Curie temperature, 473 K, is attributed to the partial formation of the B2 phase as detected by XRD. The body-centered-cubic B2 phase is a soft ferromagnet at room temperature [44]. For $Mn_{55}Al_{39}Cu_6$, the Curie temperature of the $L1_0$ phase is 591 K and the Curie temperature of the B2 phase is 487 K. For the $Mn_{55}Al_{39}Ga_6$ alloy, the two Curie temperatures are 627 K for the metastable $L1_0$ phase and 572 K for the thermodynamically stable $L1_0$ phase, which is consistent with the results of Mix *et al.* [21].

In summary, we systematically investigate the influence of the three dopants on the intrinsic magnetic properties of $Mn_{55}Al_{45-x}M_x$ alloys. Cu and Co clearly degrade the intrinsic magnetic properties, while Ga slightly improves them. Next, we discuss the preferred site occupancy of Cu, Co, and Ga, and investigate the atomic occupation and electronic structure to understand why the intrinsic magnetic properties are changed.

C. Atomic occupation analysis

The possible site occupation of doping atoms is illustrated in Figs. 6(a), 6(c), and 6(e). We build the structure with two unit cells, and accommodate one extra Mn at the 1d site. The projection drawings of the $L1_0$ lattice along the [$\bar{1}$00] direction [front view of $L1_0$ lattice in Figs. 6(a), 6(c), and 6(e)] are shown in Figs. 6(b), 6(d), and 6(f). The horizontal axis and the vertical axis of the lattices in Figs. 6(b), 6(c), and 6(f) are [010] and [001], respectively. The projection drawings are shown to make it easier to see the neighbor relationship between atoms.

As mentioned in Sec. I, the Mn atoms enter 1a sites and couple ferromagnetically, while the Al atoms and excess Mn atoms enter 1d sites. The 1d Mn interacts antiferromagnetically with the 1a Mn, as shown in Figs. 6(a) and 6(b). When a third atom M partially substitutes for Al in the structure, there are only two possibilities. It can occupy a 1d site directly, or it can displace a 1a-site Mn. Wherever there is excess Mn, the crystallographic sites become inequivalent. To simplify the analysis, we

choose just one possible position for the dopant atoms in each site. If they occupy the 1a site, the original Mn atoms at the 1a sites are displaced to the 1d-Al vacancies with reversed magnetic moments, as shown in Figs. 6(c) and 6(d). Therefore, the doped atoms entering the 1a Mn sites will cause more antiferromagnetic interactions and reduce the magnetization dramatically. If the doping atoms occupy the 1d sites, they do not change the Mn coupling, as shown in Figs. 6(e) and 6(f). The evolution of magnetization will depend on the moment of doping atoms. In view of the experimental data, we speculate the Ga atoms enter the 1d sites and the Cu and Co atoms occupy the 1a sites.

The site preferences of Cu, Co, and Ga in the $L1_0$ lattice can also be calculated from first principles. To approximate the atomic formula, Mn-Al $L1_0$ supercells are built with 36 atoms, $Mn_{20}Al_{16}$, corresponding to the composition of 55.5 at. % Mn and 44.5 at. % Al. We calculate the formation energy for each of the different nonequivalent structures of the $Mn_{20}Al_{16}$ supercell and obtain the stablest one, as shown in Fig. 7. On the basis of this structure, one dopant atom M ($M = $ Co, Cu, Ga) substitutes for one Al atom, corresponding to $Mn_{20}Al_{15}M$ with a composition of 2.8 at. % M. The two possibilities, that the M atom enters 1a sites (20 different nonequivalent structures) or the M atom enters 1d sites (four different nonequivalent structures), are calculated to predict the structure with the lowest energy. The stablest structures are shown in Fig. 7. The energies of all the structures are given in Figs. S5–S8 in Supplemental Material [17]. The results show that Co and Cu atoms prefer 1a sites, while Ga prefers 1d sites, in agreement with the experimental analysis of the magnetism.

Table I presents a summary of the atomic moments, total magnetic moments, and saturation magnetization obtained by magnetic measurements and theoretical calculations. The moments of these systems are eventually the localized Mn_{1a} and Mn_{1d} moments, with negligible contribution from Al or the dopant atoms (Co, Cu, and Ga). The good agreement between theoretical and experimental data confirms the validity of the selected crystal structure and the calculated results.
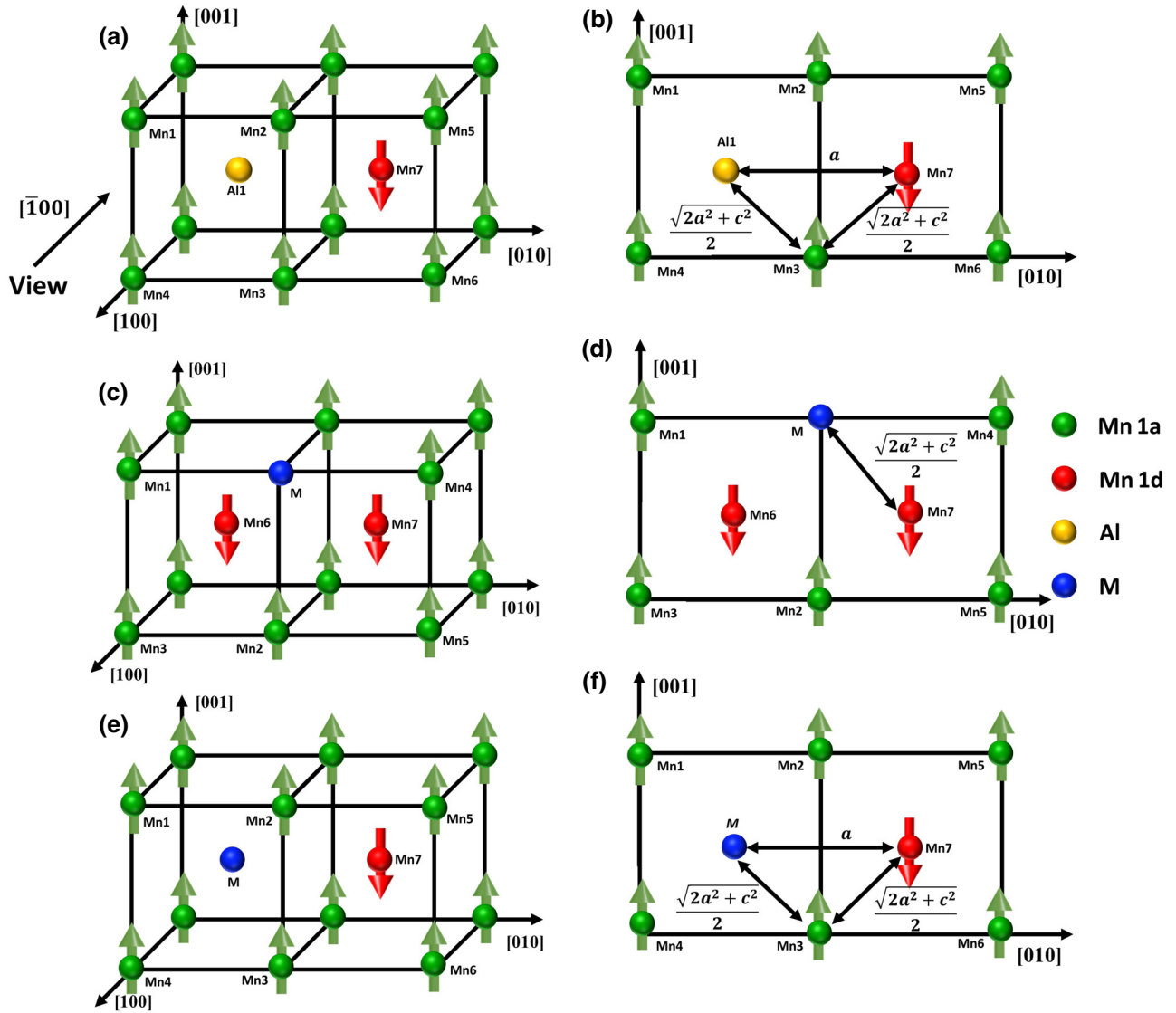
FIG. 6. (a),(b) Localized magnetic structure of the L1$_0$ phase with excess Mn atoms. Localized magnetic structure of doped alloys with doping atoms at (c),(d) the 1a site and (e),(f) the 1d site.

D. Electronic structure

The electronic structure of Mn$_{20}$Al$_{15}M$ (M = Co, Cu, Ga) is analyzed for further insight into the effect of doping with substitutional atoms on the intrinsic magnetism. The spin-polarized total density of states (DOS) and partial DOS of the L1$_0$ phase are calculated. Figures 8(a)–8(d) shows the total and partial electronic density of states of the undoped and doped alloys. All the DOS plots exhibit obvious ferromagnetic exchange splitting of more than 2 eV, confirming the ferromagnetic state observed experimentally and in accordance with previous results [4,19]. The Fermi level is located in a valley for both majority and minority bands, suggesting that these lattice structures are electronically stable [19]. More specifically, for Mn$_{20}$Al$_{16}$, the states below −4 eV are the sp states of Al;

the d states of Mn extend from −4 to +3 eV. Mn$_{1a}$ and Mn$_{1d}$ exhibit similar distributions of the DOS, but with different spin order, having strong antiferromagnetic coupling. Mn$_{1a}$ and Mn$_{1d}$ have a nearest-neighbor distance of about 2.65 Å, a value shorter than 2.8 Å, which is the critical distance for antiferromagnetic coupling of Mn atoms [6,29,50], so the Mn$_{1a}$ and Mn$_{1d}$ atoms couple antiferromagnetically. Mn$_{1a}$ and Mn$_{1d}$ atoms have different magnetic moments of about 2.4μ_B and −3.2μ_B, respectively, as listed in Table I. The absolute value of the magnetic moment of Mn$_{1a}$ is less than that of Mn$_{1d}$ because the Mn$_{1d}$ atoms have eight Mn$_{1a}$ atoms as their nearest neighbors, as in a cubic crystal field, whereas the Mn$_{1a}$ atoms have eight Al atoms or seven Al atoms and one Mn$_{1d}$ atom as their nearest neighbors [50]. Meanwhile, the
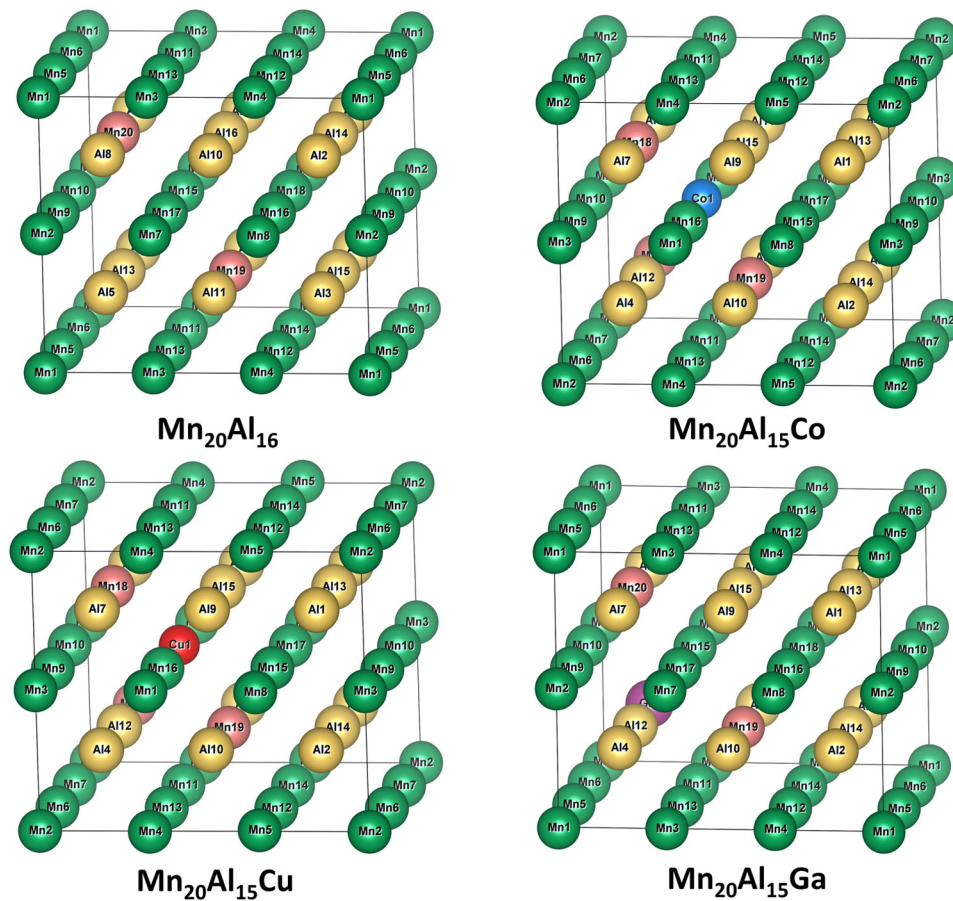
FIG. 7. Stable structures of $Mn_{20}Al_{16}$, $Mn_{20}Al_{15}Ga$, $Mn_{20}Al_{15}Cu$, and $Mn_{20}Al_{15}Co$ according to the calculated results.

Mn_{1a} atoms are covalently hybridized with Al-derived sp states; the p-d hybrid peaks of both spin-down and spin-up states are located at around -1.2 and -2.8 eV, respectively. This covalent bonding has less effect on the Mn_{1d} atoms due to the atomic separation of Al and Mn_{1d} being larger than the separation of Al and Mn_{1a} [in the lattice we chosen $a = 2.777$ Å and $c = 3.571$ Å, $r(Mn_{1a} - Al) = (\sqrt{2a^2 + c^2}/2) \approx 2.654$ Å, $r(Mn_{1d} - Al) = a \approx 2.777$ Å, so $r(Mn_{1a} - Al) < r(Mn_{1d} - Al)$, as shown in Fig. 6(b)]. The p-d hybridization makes the occupation of d states for Mn_{1a} atoms increase and thus also reduces the magnetic moment of Mn_{1a} atoms [50–52].

The total magnetic moment is the difference between the number of spin-up occupied states and the number if spin-down occupied states. For $Mn_{20}Al_{15}Co$, Co doping leads to a decrease $\Delta m_{tot} = 5.2\mu_B$ per Co atom compared with the binary Mn-Al compounds. This is mainly attributed to the more antiferromagnetic interactions caused by Co displacing a 1a-site Mn. The spin moment of Co is small and antiparallel to that of Mn_{1a}, as shown in Table I. The electronic structure and magnetism of $3d$ atoms are strongly influenced by their chemical surroundings. Co has six Al atoms and three Mn_{1d} atoms as first neighbors, and four Mn_{1a} atoms as second neighbors, as shown in Figs. 9(a) and 9(b). Firstly, the exchange between the

nearest neighbors is strongest, so the direct interactions between Mn_{1d} and Co make the magnetic moment of Co negative. Furthermore, the covalent d-d hybridization peaks of Co and Mn_{1d} and Co and Mn_{1a} can be found at -2.7 and -1.2 eV, respectively, and Co atoms ($3d^7s^2$) have more valence electrons than Mn atoms ($3d^5s^2$). Because higher-valence transition atoms (Co) generally have lower-energy d-states than the lower-valence atoms (Mn), the bonding states tend to localize on Co below the Fermi level for both spin-up and spin-down states, whereas the antibonding density is relatively small above the Fermi level. This means the exchange splitting of Co is weakened, resulting in the small moment of Co. Meanwhile, the p-d hybridization peaks between Co and Al atoms of both spin-up and spin-down states are observed at -1.2 eV. This p-d hybridization also keeps the energy level of Co completely locked below the Fermi level to inhibit the spin polarization. This is the other reason for the small value of the calculated magnetic moment of Co atoms. Furthermore, this hybridization causes Co to occupy 1a sites that are nearest to Al atoms [52,53]. The specific variation of d states is summarized in Figs. 9(c) and 9(d).

Figure 8(c) shows the electronic structure for Cu-doped alloys. The density of states of Cu is mainly localized around -3.5 eV; Cu atoms do not exhibit
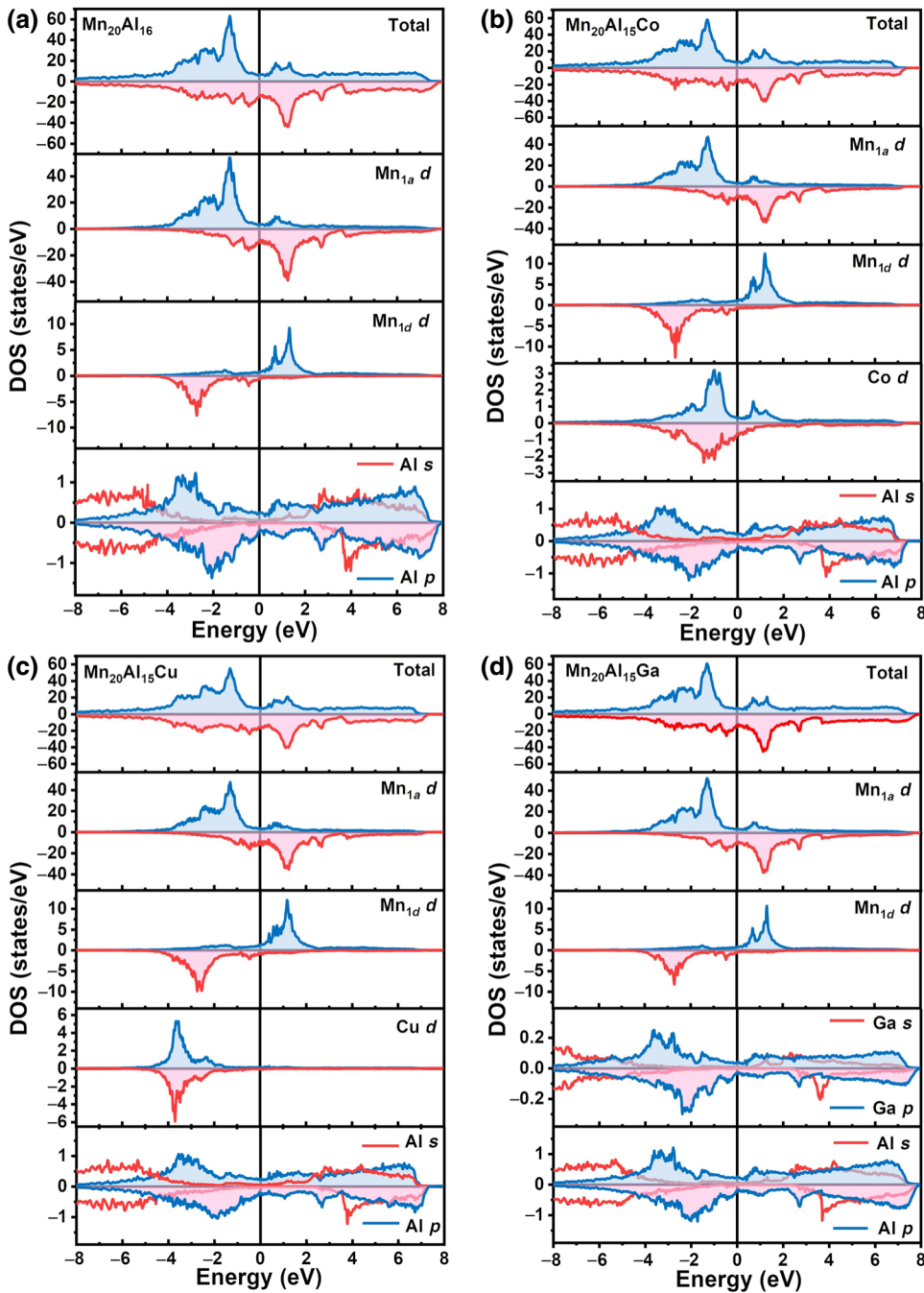
FIG. 8. Calculated total and partial DOS of (a) $Mn_{20}Al_{16}$, (b) $Mn_{20}Al_{15}Co$, (c) $Mn_{20}Al_{15}Cu$, and (d) $Mn_{20}Al_{15}Ga$.

strong hybridization with their neighboring atoms. This is attributed to Cu atoms having a filled $3d$ shell ($3d^{10}4s^1$). However, the p-d hybridization is between Cu and Al atoms located at -3.6 eV. This shows that Cu atoms tend to enter 1a sites, similarly to Co atoms. In Fig. 8(d), the calculated total DOS and partial DOS of $Mn_{20}Al_{15}Ga$ are shown. The p-d-hybrid peaks of Ga atoms are close to those of Al atoms, suggesting that Ga atoms have almost the same effects as Al regarding p-d hybridization.

In summary, Co and Cu with more valence electrons than Mn prefer 1a sites due to the strong p-d hybridization

with Al, while Ga tends to occupy 1d sites due to its valence-electron structure being similar to that of Al. On the basis of our results and previous literature, $3d$ elements with more valence electrons than Mn tend to enter 1a sites due to their stronger p-d hybridization with Al than Mn, while elements with fewer valence electrons than Mn atoms prefer 1d sites [50–53]. Therefore, on the basis of our analysis, if we want to improve the magnetic properties of binary Mn-Al alloys, we should decrease the number of antiferromagnetic Mn atoms by doping them with atoms that substitute for Mn, and the substitutional atoms need

TABLE I. The average magnetic moments of Mn_{1a}, Mn_{1d}, Al, and M, the total magnetic moment of $Mn_{20}Al_{16}$ and $Mn_{20}Al_{15}M$ (M = Co, Cu and Ga), and the calculated and experimental values of the saturation magnetization.

Quantity	$Mn_{20}Al_{16}$ ($Mn_{55.5}Al_{44.5}$)	$Mn_{20}Al_{15}Co$ ($Mn_{55.5}Al_{41.7}Co_{2.8}$)	$Mn_{20}Al_{15}Cu$ ($Mn_{55.5}Al_{41.7}Cu_{2.8}$)	$Mn_{20}Al_{15}Ga$ ($Mn_{55.5}Al_{41.7}Ga_{2.8}$)
$\mu_{Mn_{1a}}$ (μ_B)	2.438	2.454	2.432	2.442
$\mu_{Mn_{1d}}$ (μ_B)	−3.176	−3.136	−3.167	−3.179
μ_{Al} (μ_B)	−0.060	−0.056	−0.056	−0.060
μ_M (μ_B)	...	−0.301	−0.036	−0.132
μ_{tot} (μ_B/f.u.)	36.988	31.8019	31.178	36.942
M_s^{cal} (MA/m)	0.692	0.595	0.583	0.691
M_s^{expt} (MA/m)	0.646 ($Mn_{55}Al_{45}$)	0.543 ($Mn_{55}Al_{43}Co_2$)	0.507 ($Mn_{55}Al_{42}Cu_3$)	0.634 ($Mn_{55}Al_{42}Ga_3$)

f.u., formula unit.

to enter 1d sites (antiferromagnetic Mn vacancies). Therefore, a possible strategy to increase the magnetization is to substitute light 3d atoms (such as Ti and V) for the antiferromagnetic Mn atoms, but the preparation method and phase stability of the thus-alloyed $L1_0$ phase still need to be explored [32].

E. Thermal stability

The thermal stability of the $L1_0$ phase for undoped and doped alloys is investigated by aging treatment

and subsequent magnetic measurements. The binary $Mn_{55}Al_{45}$ and ternary $Mn_{55}Al_{43}Co_2$, $Mn_{55}Al_{42}Cu_3$, and $Mn_{55}Al_{42}Ga_3$ specimens are isothermally aged at 923 K for 0, 5, 10, and 15 h, respectively. Then magnetization curves of the treated specimens are measured at 300 K, as shown in Figs. 10(a)–10(d). Since $L1_0$ is the sole ferromagnetic phase for $Mn_{55}Al_{45-x}M_x$ (M = Co, Cu, Ga) alloys, the parameter M_t/M_0 can accurately reflect the remaining fraction of the $L1_0$ phase, where M_t and M_0 represent the magnetization of the specimens annealed for different times and the magnetization of the unannealed specimens,
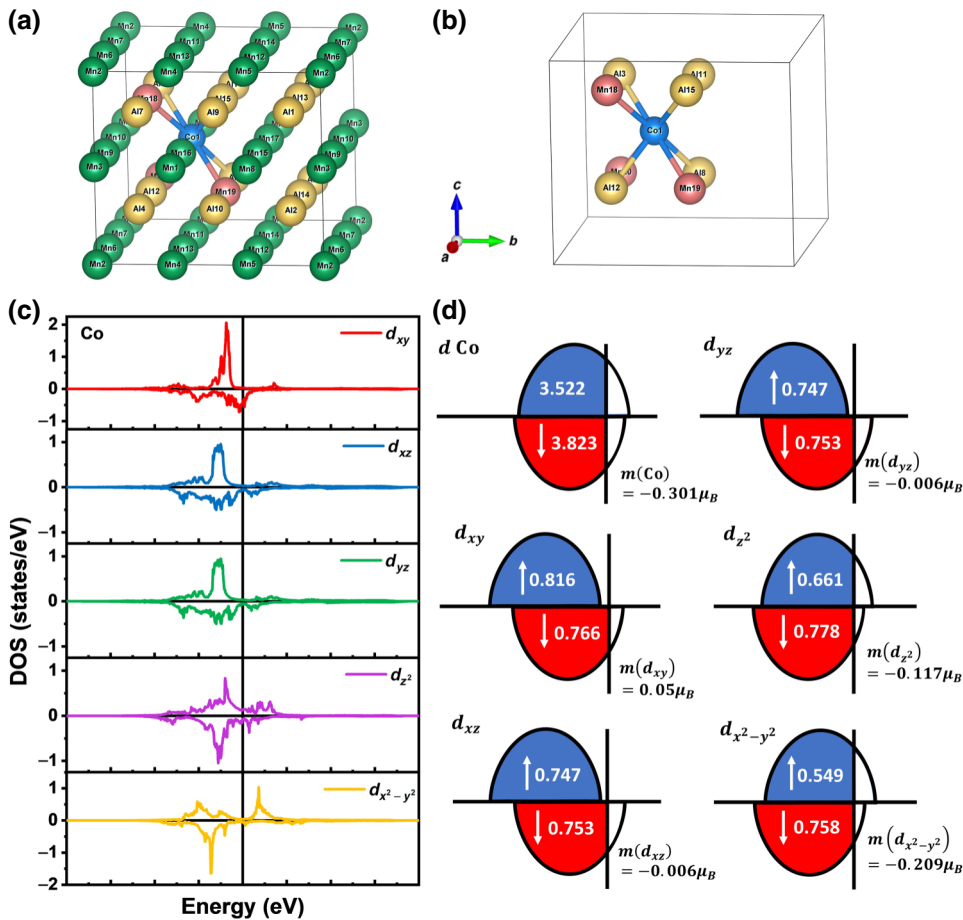

FIG. 9. (a) The stable structure of $Mn_{20}Al_{15}Co$. (b) First-neighbor environment of the Co atom. (c) The typical partial DOS of Co 3d. (d) Density-of-states diagram showing the variation of d states in $Mn_{20}Al_{15}Co$.
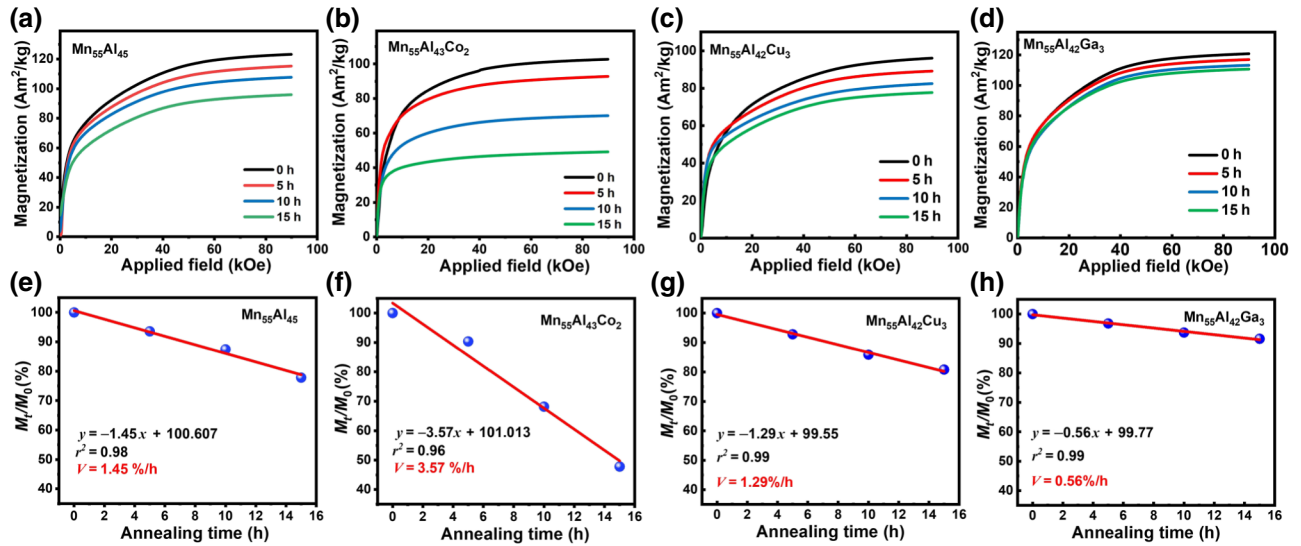
FIG. 10. M-H curves measured at 300 K for (a) $Mn_{55}Al_{45}$, (b) $Mn_{55}Al_{43}Co_2$, (c) $Mn_{55}Al_{42}Cu_3$, and (d) $Mn_{55}Al_{42}Ga_3$ alloys annealed for different times. Linear-fit curves of M_t/M_0 versus annealing time for (e) $Mn_{55}Al_{45}$, (f) $Mn_{55}Al_{43}Co_2$, (g) $Mn_{55}Al_{42}Cu_3$, and (h) $Mn_{55}Al_{42}Ga_3$ alloys.

respectively. The dependence of M_t/M_0 on aging time is summarized in Figs. 10(e)–10(h). M_t/M_0 shows a perfect linear relationship with aging time, the linear-regression coefficient (r^2) being more than 0.95. Therefore, the slope gives the decomposition rate of the $L1_0$ phase. The decomposition rates of the $L1_0$ phase of binary $Mn_{55}Al_{45}$ and Co-doped, Cu-doped, and Ga-doped alloys are 1.45%/h, 3.57%/h, 1.29%/h, and 0.56%/h, respectively. That means the addition of Co degrades the stability of the $L1_0$ phase, the addition of Cu or Ga can improve the stability of the $L1_0$ phase, and Ga has the best effect among the three different dopant atoms.

IV. CONCLUSIONS

(1) A high-purity $L1_0$ phase is obtained in binary and M-alloyed ($M =$ Co, Cu, Ga) Mn-Al alloys by our optimizing the preparation method, and the effect of elemental doping is investigated experimentally. The substitution of Co or Cu atoms for Al atoms by obviously decreases all the intrinsic magnetic properties (M_s, K_1, T_C), while Ga dopant has a slightly positive effect on them.

(2) The site preference of M atoms in the $L1_0$ Mn-Al lattice is analyzed by a combination of experimental results and theoretical calculations. Co and Cu atoms tend to occupy 1a (0, 0, 0) sites and displace the original Mn from 1a sites to 1d (1/2, 1/2, 1/2) sites, resulting in more Mn_{1a}-Mn_{1d} antiferromagnetic interactions and a reduction in the magnetization. Ga atoms prefer to enter 1d sites, where they cannot alter the Mn coupling conditions, and they change the intrinsic magnetism only slightly.

(3) The valence-electron structure determines the site preference of the substitutional atoms. Co and Cu have

more valence electrons than Mn, resulting in their preferential occupancy of 1a (0, 0, 0) sites. Ga has a valence-electron structure similar to that of Al, so it tends to interact with Mn, which makes it prefer 1d (1/2, 1/2, 1/2) sites.

(4) A possible strategy to improve the intrinsic magnetic properties is to substitute $3d$ atoms with fewer valence electrons for the antiferromagnetic Mn atoms, but the preparation method and the phase stability of such alloyed $L1_0$ phases with high purity require further investigation.

(5) Both Ga and Cu as dopants can stabilize the metastable $L1_0$ phase compared with the binary Mn-Al alloy, but the addition of Co degrades the stability of the $L1_0$ phase significantly.

[1] M. J. Kramer, R. W. McCallum, I. A. Anderson, and S. Constantinides, Prospects for non-rare earth permanent magnets for traction motors and generators, J. Miner. Met. Mater. Soc. **64**, 752 (2012).

[2] L. H. Lewis and F. Jiménez-Villacorta, Perspectives on permanent magnetic materials for energy conversion and power generation, Metall. Mater. Trans. A **44**, 2 (2012).

[3] J. H. Park, Y. K. Hong, S. Bae, J. J. Lee, J. Jalli, G. S. Abo, N. Neveu, S. G. Kim, C. J. Choi, and J. G. Lee, Saturation magnetization and crystalline anisotropy calculations for MnAl permanent magnet, J. Appl. Phys. **107**, 09A731 (2010).

[4] A. Edström, J. Chico, A. Jakobsson, A. Bergman, and J. Rusz, Electronic structure and magnetic properties of L1₀ binary alloys, Phys. Rev. B **90**, 014402 (2014).

[5] A. Sakuma, Electronic structure and magnetocrystalline anisotropy energy of MnAl, J. Phys. Soc. Jpn **63**, 1422 (1994).

[6] J. M. D. Coey, New permanent magnets; manganese compounds, J. Phys.: Condens. Matter **26**, 064211 (2014).

[7] J. M. D. Coey, Permanent magnets: Plugging the gap, Scr. Mater. **67**, 524 (2012).

[8] R. Skomski and J. M. D. Coey, Magnetic anisotropy - How much is enough for a permanent magnet?, Scr. Mater. **112**, 3 (2016).

[9] J. M. D. Coey, Hard magnetic materials: a perspective, IEEE Trans. Magn. **47**, 4671 (2011).

[10] J. Cui, M. Kramer, L. Zhou, F. Liu, A. Gabay, G. Hadjipanayis, B. Balasubramanian, and D. Sellmyer, Current progress and future challenges in rare-earth-free permanent magnets, Acta Mater. **158**, 118 (2018).

[11] T. L. Zhang, H. Y. Liu, J. H. Liu, and C. B. Jiang, 2:17-type SmCo quasi-single-crystal high temperature magnets, Appl. Phys. Lett. **106**, 162403 (2015).

[12] Q. Y. Wang, L. Zheng, S. Z. An, T. L. Zhang, and C. B. Jiang, Thermal stability of surface modified Sm₂Co₁₇-type high temperature magnets, J. Magn. Magn. Mater. **331**, 245 (2013).

[13] A. J. J. Koch, P. Hokkeling, M.G.v.d. Steeg, and K. J. de Vos, New material for permanent magnets on a base of Mn and Al, J. Appl. Phys. **31**, 75S (1960).

[14] H. Kono, On the Ferromagnetic Phase in manganese-aluminum system, J. Phys. Soc. Jpn **13**, 1444 (1958).

[15] D. Palanisamy, D. Raabe, and B. Gault, Elemental segregation to twin boundaries in a MnAl ferromagnetic Heusler alloy, Scr. Mater. **155**, 144 (2018).

[16] F. Bittner, J. Freudenberger, L. Schultz, and T. G. Woodcock, The impact of dislocations on coercivity in L1₀-MnAl, J. Alloy. Compd. **704**, 528 (2017).

[17] See Supplemental Material at http://link.aps.org/supplemental/10.1103/PhysRevApplied.11.064008 for a schematic diagram of the structure transformation from FCT to BCT of the τ phase, and the XRD patterns, a summary of the heat treatment, the phase structures, the lattice structures, the chemical compositions, and the calculated formation energies of Co-, Cu-, and Ga-doped Mn-Al alloys.

[18] J. Z. Wei, Z. G. Song, Y. B. Yang, S. Q. Liu, H. L. Du, J. Z. Han, D. Zhou, C. S. Wang, Y. C. Yang, A. Franz, D. TÓğbbens, and J. B. Yang, τ-MnAl with high coercivity and saturation magnetization, AIP Adv. **4**, 127113 (2014).

[19] K. Anand, J. J. Pulikkotil, and S. Auluck, Study of ferromagnetic instability in τ-MnAl, using first-principles, J. Alloy. Compd. **601**, 234 (2014).

[20] V. T. Nguyen, F. Calvayrac, A. Bajorek, and N. Randrianantoandro, Mechanical alloying and theoretical studies of MnAl(C) magnets, J. Magn. Magn. Mater. **462**, 96 (2018).

[21] T. Mix, F. Bittner, K.-H. Müller, L. Schultz, and T. G. Woodcock, Alloying with a few atomic percent of Ga makes MnAl thermodynamically stable, Acta Mater. **128**, 160 (2017).

[22] F. Bittner, L. Schultz, and T. G. Woodcock, Twin-like defects in L1₀ ordered τ-MnAl-C studied by EBSD, Acta Mater. **101**, 48 (2015).

[23] Q. Zeng, I. Baker, J. B. Cui, and Z. C. Yan, Structural and magnetic properties of nanostructured Mn-Al-C magnetic materials, J. Magn. Magn. Mater. **308**, 214 (2007).

[24] E. Fazakas, L. K. Varga, and F. Mazaleyrat, Preparation of nanocrystalline Mn-Al-C magnets by melt spinning and subsequent heat treatments, J. Alloy. Compd. **434–435**, 611 (2007).

[25] J. H. Huang and P. C. Kuo, Influence of carbon on the phase transformation kinetics and magnetic properties of Mn-A1 alloys, Mater. Sci. Eng. B **22**, 256 (1994).

[26] H. L. Fang, J. Cedervall, F. J. M. Casado, Z. Matej, J. Bednarcik, J. ÅngstrÓğm, P. Berastegui, and M. Sahlberg, Insights into formation and stability of τ-MnAlZₓ (Z = C and B), J. Alloy. Compd. **692**, 198 (2017).

[27] S. Zhao, Y. Y. Wu, C. Zhang, J. M. Wang, Z. H. Fu, R. F. Zhang, and C. B. Jiang, Stabilization of τ-phase in carbon-doped MnAl magnetic alloys, J. Alloy. Compd. **755**, 257 (2018).

[28] P. Z. Si, H. D. Qian, C. J. Choi, J. Park, and H. L. Ge, A novel method for measuring the phase transformation temperature and enhanced coercivity in cold-rolled MnAlCₓ (x = 0 - 5) alloys, J. Magn. Magn. Mater. **451**, 540 (2018).

[29] L. Pareti, F. Bolzoni, F. Leccabue, and A. E. Ermakov, Magnetic anisotropy of MnAl and MnAlC permanent magnet materials, J. Appl. Phys. **59**, 3824 (1986).

[30] S. Zhao, Y. Y. Wu, J. M. Wang, Y. X. Jia, T. L. Zhang, T. L. Zhang, and C. B. Jiang, Improved coercivity in MnAl permanent-magnet alloys by introducing nanoprecipitates, J. Magn. Magn. Mater. **483**, 164 (2019).

[31] S. Mican, D. Benea, R. Hirian, R. Gavrea, O. Isnard, V. Pop, and M. Coldea, Structural, electronic and magnetic properties of the Mn₅₀Al₄₆Ni₄ alloy, J. Magn. Magn. Mater. **401**, 841 (2016).

[32] R. Gavrea, R. Hirian, S. Mican, D. Benea, O. Isnard, M. Coldea, and V. Pop, Structural, electronic and magnetic properties of the Mn₅₄₋ₓAl₄₆Tiₓ (x = 2; 4) alloys, Intermetallics **82**, 101 (2017).

[33] P. Manchanda, A. Kashyap, J. E. Shield, L. H. Lewis, and R. Skomski, Magnetic properties of Fe-doped MnAl, J. Magn. Magn. Mater. **365**, 89 (2014).

[34] P. Manchanda, P. Kumar, A. Kashyap, M. J. Lucis, J. E. Shield, A. Mubarok, J. I. Goldstein, S. Constantinides, K. Barmak, L. H. Lewis, D. J. Sellmyer, and R. Skomski, Intrinsic properties of Fe-substituted magnets, IEEE Trans. Magn. **49**, 5194 (2013).

[35] W. B. Pearson, *The crystal chemistry and physics of metals and alloys* (Wiley, New York, 1972).

[36] M. Sugihara and I. Tsuboya, Structural and magnetic properties of copper-substituted manganese - aluminum alloys, J. Appl. Phys. **330**, 1338 (1962).

[37] H. Zhao, W. Y. Yang, Z. Y. Shao, G. Tian, D. Zhou, X. P. Chen, Y. H. Xia, L. Xie, S. Q. Liu, H. L. Du, J. Z. Han, C. S. Wang, Y. C. Yang, and J. B. Yang, Structural evolution and magnetic properties of $L1_0$-type $Mn_{54.5}Al_{45.5-x}Ga_x$ (x = 0.0, 15.0, 25.0, 35.0, 45.5) phase, J. Alloy. Compd. **680**, 14 (2016).

[38] G. Kresse and J. Furthmüller, Efficiency of ab-initio total energy calculations for metals and semiconductors using a plane-wave basis set, Comp. Mater. Sci. **6**, 15 (1996).

[39] G. Kresse and D. Joubert, From ultrasoft pseudopotentials to the projector augmented-wave method, Phys. Rev. B **59**, 1758 (1999).

[40] J. P. Perdew, K. Burke, and M. Ernzerhof, Generalized Gradient Approximation Made Simple, Phys. Rev. Lett. **77**, 3865 (1996).

[41] A. D. Crisan, F. Vasiliu, R. Nicula, C. Bartha, I. Mercioniu, and O. Crisan, Thermodynamic, structural and magnetic studies of phase transformations in MnAl nanocomposite alloys, Mater. Charact. **140**, 1 (2018).

[42] W. Lu, J. C. Niu, T. L. Wang, K. Xia, Z. Xiang, Y. M. Song, Z. L. Mi, W. F. Zhang, W. Tian, and Y. Yan, Phase transformation kinetics and microstructural evolution of MnAl permanent magnet alloys, J. Alloy. Compd. **685**, 992 (2016).

[43] G. Effenberg, S. Ilyenko, and O. Dovbenko, *Ternary Alloy Systems* (Springer-Verlag, Berlin, 2009).

[44] C. Paduani, J. Schaf, A. I. C. Persiano, J. D. Ardisson, A. Y. Takeuchi, and I. C. Riegel, Strong dependence of ferrimagnetic properties on Co concentration in the $Mn_{1-x}Al_{1-y}Co_{x+y}$ system, Intermetallics **18**, 1659 (2010).

[45] I. Tsuboya and M. Sugihara, The magnetic properties of the κ phase in Mn-Al-Co system, J. Phys. Soc. Jpn **17**, 410 (1962).

[46] G. Hadjipanayis, D. J. Sellmyer, and B. Brandt, Rare-earth-rich metallic glasses. I. Magnetic hysteresis, Phys. Rev. B **23**, 3349 (1981).

[47] T. Mix, K.-H. Müller, L. Schultz, and T. G. Woodcock, Formation and magnetic properties of the $L1_0$ phase in bulk, powder and hot compacted Mn-Ga alloys, J. Magn. Magn. Mater. **391**, 89 (2015).

[48] Y. Huh, P. Kharel, A. Nelson, V. R. Shah, J. Pereiro, P. Manchanda, A. Kashyap, R. Skomski, and D. J. Sellmyer, Effect of Co substitution on the magnetic and electron-transport properties of Mn_2PtSn, J. Phys.: Condens. Matter **27**, 076002 (2015).

[49] C. Zhang, T. L. Zhang, J. M. Wang, S. Zhao, Y. Y. Wu, and C. B. Jiang, Anisotropic single-variant of $(Mn_{54}Al_{46})_{97}C_3$, Scr. Mater. **143**, 72 (2018).

[50] H. Z. Luo, Z. Y. Zhu, L. Ma, S. F. Xu, X. X. Zhu, C. B. Jiang, H. B. Xu, and G. H. Wu, Effect of site preference of $3d$ atoms on the electronic structure and half-metallicity of Heusler alloy Mn_2YAl, J. Phys. D: Appl. Phys. **41**, 055010 (2008).

[51] L. Ma, W. H. Wang, C. M. Zhen, D. L. Hou, X. D. Tang, E. K. Liu, and G. H. Wu, Polymorphic magnetization and local ferromagnetic structure in Co-doped Mn_2NiGa alloys, Phys. Rev. B **84**, 224404 (2011).

[52] T. J. Burch, T. Litrenta, and J. I. Budnick, Hyperfine Studies of Site Occupation in Ternary Systems, Phys. Rev. Lett. **33**, 421 (1974).

[53] I. Galanakis, P. H. Dederichs, and N. Papanikolaou, Origin and properties of the gap in the half-ferromagnetic Heusler alloys, Phys. Rev. B **66**, 134428 (2002).